Spectral Reflectance and Atmospheric Energetics in Cirrus-like Clouds. Part II: Applications of a Fourier–Riccati Approach to Radiative Transfer

SI-CHEE TSAY

Laboratory for Atmospheres, NASA/Goddard Space Flight Center, Greenbelt, Maryland

PHILIP M. GABRIEL

Department of Atmospheric Science, Colorado State University, Fort Collins, Colorado

MICHAEL D. KING

Earth Sciences Directorate, NASA/Goddard Space Flight Center, Greenbelt, Maryland

GRAEME L. STEPHENS

Department of Atmospheric Science, Colorado State University, Fort Collins, Colorado

ABSTRACT

One of the major sources of uncertainty in climate studies is the detection of cirrus clouds and characterization of their radiative properties. Combinations of water vapor absorption channels (e.g., 1.38 μm), ice–water absorption channels (e.g., 1.64 μm), and atmospheric window channels (e.g., 11 μm) in the imager, together with a lidar profiler on future EOS platforms, will contribute to enhancing our understanding of cirrus clouds.

The aforementioned spectral channels are used in this study to explore the effects exerted by uncertainties in cloud microphysical properties (e.g., particle size distribution) and cloud morphology on the apparent radiative properties, such as spectral reflectance and heating and cooling rate profiles. As in Part I of our previous study, which establishes the foundations of the Fourier–Riccati method of radiative transfer in inhomogeneous media, cloud extinction and scattering functions are characterized by simple spatial variations with measured and hypothesized microphysics to facilitate our understanding of their radiative properties.

Results of this study suggest that (i) while microphysical variations in the scattering and extinction functions of clouds affect the magnitudes of their spectral reflectances, cloud morphology significantly alters the shape of their angular distribution; (ii) spectral reflectances viewed near nadir are least affected by cloud variability; and (iii) cloud morphology can lead to spectral heating and cooling rate profiles that differ substantially from their plane–parallel averaged equivalents. Since there are no horizontal thermal gradients in plane-parallel clouds, it may be difficult to correct for this deficiency.

1. Introduction

Cirrus clouds are characterized by their large areal extent and long persistence. As such, these clouds strongly modulate the radiative energy exchange in the earth–atmosphere system and are a significant component of the earth's climate (cf. Liou 1986 for a detailed review). In spite of the importance of cirrus clouds, our understanding of them is made difficult by their relative inaccessibility. Recently, our knowledge of these clouds has been considerably expanded through various national and international research programs. For example, FIRE [First ISCCP (International Satellite Cloud Climatology Project) Regional Experiment] fostered extensive work detailing the composition, dynamics, and thermodynamics that are responsible for the formation, maintenance, and decay of cirrus clouds (cf. special issue of *Monthly Weather Review,* Vol. 118, No. 11, 1990).

One important issue raised from the FIRE-86 Cirrus Intensive Field Observations (IFO) was the substantial disagreement between in situ measurements of cloud properties (e.g., effective particle radius, optical thickness) and those retrieved by remote sensing. Many explanations have been proposed to account for the large disparities in the effective particle radius. Two of the most common hypotheses were that (i) cirrus clouds contain a large number of small particles not resolvable

Corresponding author address: Dr. Si-Chee Tsay, Laboratory for Atmospheres, NASA/Goddard Space Flight Center, Code 913, Greenbelt, MD 20771.
E-mail: tsay@climate.gsfc.nasa.gov

by the then state-of-the-art instrumentation that was in-capable of detecting particles in the $20-50$ μm range, depending on aircraft speed (Heymsfield et al. 1990), and (ii) the simplistic treatment of complex particle shapes and uncertainties in the refractive index of ice (e.g., Wielicki et al. 1990; Sassen et al. 1990). The significance of this disagreement can be appreciated in the context of climate simulations (e.g., Stephens et al. 1990) that pointed to a sensitivity of climate to the microphysics of cirrus clouds. Therefore, predictions at this time concerning cirrus cloud feedback on climate are premature in view of our lack of understanding of the relationships between cirrus cloud microphysics and the gross radiative characteristics of these clouds.

Based on the findings of FIRE-86, a second phase (FIRE-91) was initiated to address questions concerning the life cycle of cirrus clouds in far greater detail. In this connection, two particular objectives of FIRE-91 (FIRE Phase II: Cirrus Implementation Plan 1990) were (i) to assess the manner by which cirrus clouds and cloud systems interact with their environment and hence affect climate, and (ii) to assess the capabilities of future cloud-radiation observing systems, such as the Earth Observing System (EOS; Price et al. 1993). These problems fall to a large extent within the domain of radiative transport under the general categories of energetics and remote sensing, respectively. The common element of either category that is relevant to this study is the correct accounting of cloud morphology in radiative processes in the atmosphere. The prospects for advancing our knowledge of cirrus cloud morphology will be enriched by coordinating data obtained from advanced observation platforms in concert with sophisticated radiative transfer models. Under EOS, data provided by the Moderate Resolution Imaging Spectroradiometer (MODIS; Salomonson et al. 1989; King et al. 1992) and the Clouds and the Earth's Radiant Energy System (CERES), in combination with data obtained from the Geoscience Laser Altimeter System (GLAS; Spinhirne et al. 1991), can be used to aid significantly cloud, radiation, and climate studies (Wielicki et al. 1995).

The need to understand and model how cloud variability affects radiative transfer is rooted on two premises. The first is that satellite data are and will continue to be extremely useful quantitatively for the remote sensing of the atmosphere and as an aid in addressing weather-related and climatological issues. In a more qualitative sense, satellite data also provide subjective cues for assessing the global meteorological situation that cannot be obtained in any other way. The second premise is that in situ measurements of cloud microphysical and radiative properties might provide for an increase in our knowledge of clouds and the dynamical processes responsible for their evolution. A physically correct interpretation of the radiometric data for the purposes mentioned above places requirements on radiative transfer models. An important feature of radi-ative transfer models is that they should accommodate the spatial variability of cirrus clouds (or other kinds of clouds) inherent in the data and calculate radiation fields that are in some sense consistent with those that are measured. To date, most radiative transfer calculations continue to disregard the importance of cloud structure by neglecting correlations in the optical properties of clouds (e.g., independent pixel calculations) or have attempted to incorporate cloud inhomogeneity simply by employing cloud fractions in concert with plane-parallel computations. Some of the side effects induced by such procedures on simulated cloud morphologies (e.g., erroneous spatial distributions of flux and radiance) have already been discussed in the literature (e.g., Gabriel et al. 1993; Evans 1993; Cahalan et al. 1994). The effects exerted by inhomogeneities in cloud optical properties on domain-averaged net fluxes have been addressed by Gabriel and Evans (1996). The main focus of the present study is to examine the effects of cloud morphology and cloud microphysics on (i) angular distribution of reflected radiance fields and (ii) heating and cooling rate profiles.

We begin this study by showing horizontal and vertical cross sections of cirrus clouds obtained from advanced remote-sensing instrumentation. A brief discussion of these instruments is also provided. The images physically represent a radiance field created by radiative processes acting on clouds present within a certain volume of the atmosphere. The ambiguities present in the interpretation of the radiances will be discussed in section 2. In section 3, the radiative transfer model and its limitations are summarized, leaving details of the extensions of the model described in Part I to the appendix. Then various assumptions used in simulations that address the way in which cloud microphysics and morphology affect the radiation field are discussed. Section 4 provides a detailed analysis of reflectances and radiative heating and cooling rates for cirrus-like cloud distributions in three spectral bands. Finally, our findings of the effects of cloud microphysics and morphology on cirrus radiative properties are summarized in section 5.

2. Observations: The FIRE-91 Cirrus IFO

During the FIRE-91 Cirrus IFO, active and passive radiometers were flown on the NASA ER-2 aircraft to remotely sense cirrus clouds from an altitude of about 20 km. Twelve ER-2 missions, coordinated with three in situ aircraft and numerous satellite overpasses, were conducted between 12 November and 7 December 1991. Here we focus discussion on data obtained from the MODIS Airborne Simulator (MAS) and the Cloud Lidar System (CLS). Other instrumentation and corresponding results are described elsewhere.

The MAS is a cross-track scanning spectrometer, built by Dædalus Enterprises for NASA Goddard Space Flight Center and Ames Research Center for measuring

reflected solar and emitted thermal radiation in 50 narrow bandwidth channels between 0.55 μm and 14.3 μm. FIRE-91 was the first deployment of this sensor that consisted of 43 spectral channels at that time, only 11 of which were recorded due to restriction imposed by the data system. Nineteen channels of the current 50-channel MAS have corresponding spectral characteristics on MODIS (cf. Salomonson et al. 1989; King et al. 1992), a satellite sensor being developed for EOS AM-1 for launch in June 1998. The MAS has a 2.5-mrad instantaneous field of view and scans perpendicularly to the aircraft flight track with a scan angle of $\pm43°$ about nadir, thereby providing images with a spatial resolution of 50 m at nadir and a 37-km swath width from the nominal ER-2 aircraft altitude of 20 km. The scan rate of the MAS is 6.25 Hz (375 rpm), which, at the nominal aircraft speed of 206 m s^{-1}, results in a 34% oversampling of contiguous scan lines along the flight track. Further information describing the optics, electronics, data-acquisition system, in-flight performance, and calibration of this instrument can be found in King et al. (1996).

The CLS is a monostatic lidar that operates in the nadir direction. Backscattered signals are acquired at the Nd:YAG laser wavelengths of 0.532 and 1.064 μm, with a pulse repetition rate of 10 pulses per second. This allows measurements to be taken at 20-m horizontal intervals at the nominal ER-2 aircraft speed. The highest attainable vertical sampling resolution is 7.5 m. Additional details of the optics, electronics, calibration, and data reduction scheme can be found in Spinhirne et al. (1982, 1996). The CLS is an airborne prototype of GLAS, a satellite sensor currently under development for EOS Laser-Altimetry to be launched in the early 2000s.

The FIRE-91 Cirrus IFO was conducted principally around Coffeyville, Kansas. The NASA ER-2 was based in Houston, Texas. We have chosen one of the ER-2 flight lines on 5 December 1991 to illustrate the complex structural features of cirrus clouds. Figure 1a shows a MAS image acquired over the Gulf of Mexico and nearby coast of Texas, processed as a three-channel red–green–blue (RGB) composite using the 2.14-μm, 1.93-μm, and 0.68-μm channels, respectively. The 2.14-μm spectral band was selected because surface reflectance is high at this wavelength and hence land features are clearly emphasized. At 1.93 μm there is a strong water vapor absorption band that helps to distinguish the lower troposphere from the radiative signatures associated with the high-level clouds. Finally, the visible channel at 0.68 μm serves to delineate the reflectance of the ocean from other features in the scene. To correct for geometric distortions generated by viewing geometry and small changes in the ER-2 ground speed, a resampling scheme was applied that yields 582 (out of 716) pixels across track with 64-m pixel spacing both along and across track. This produces a total domain size of about 37 km by 64 km for Fig. 1a.

In Fig. 1a, cirrus clouds, highlighted in green, dominate the scene. Local apparent scene brightness and texture provide for a contextual reference that affects perceptions about the optical properties of the cloud. For example, stretching the color lookup tables dramatically changes the relative brightness of the clouds. This change of brightness may be interpreted as due to differences in optical thickness. Using 11 μm instead of 2.14 μm as the red channel in the RGB composite also changes the contrast between background and clouds significantly; the contrast of cirrus clouds over land become more pronounced, whereas that of thin cirrus clouds over the oceans is almost nondetectable (figure not shown). Therefore, information pertaining to cloud structure obtained from passive radiometers is qualitative in as much as it affects the inferred optical properties of the clouds; and good calibration and a larger number of spectral channels than commonly found on operational satellites are both required to narrow uncertainties in cloud optical properties and microphysical analyses.

Figure 1b illustrates a CLS vertical profile (1.064-μm attenuated backscatter intensity) of cirrus clouds acquired along the nadir track down the center of the MAS image (yellow line down the center of Fig. 1a). Since cirrus clouds are typically optically thin, the lidar-attenuated backscatter signals are useful in determining cloud-top heights as well as the position of multiple cloud layers if present in a vertical column of the atmosphere. Multiple layers of cirrus clouds were clearly detected by CLS on this flight track, as evidenced by relatively thin cirrus clouds observed between about 11 and 12 km, together with thicker and more inhomogeneous clouds between about 7 and 9 km. It should be noted that the strength of the cirrus attenuated backscattered intensity shown in Fig. 1b will appear to change in a manner that depends on how the color lookup table is stretched.

Combining data obtained from a passive scanning imager and an active lidar system provides an invaluable tool for detecting the presence of cirrus clouds, for distinguishing their thermodynamic phase, and for testing and guiding the development of operational cloud-masking algorithms. While radiances provide useful measures of the radiative interactions, information contained in these radiance fields can only be used to make qualitative inferences about the properties of the cloud unless an appropriate radiative transfer theory is devised to invert these radiance fields. Characterizing the morphology of clouds (especially cirrus clouds) for the purpose of performing radiative transfer computations is a difficult problem, as is apparent from a careful examination of Fig. 1. From previous studies (e.g., Gabriel et al. 1993 and references therein), it is expected that the radiative properties of clouds are sensitive to cloud morphology. In view of the diversity and complexity of naturally occurring cloud systems, we elected to use a relatively simple cloud morphology on
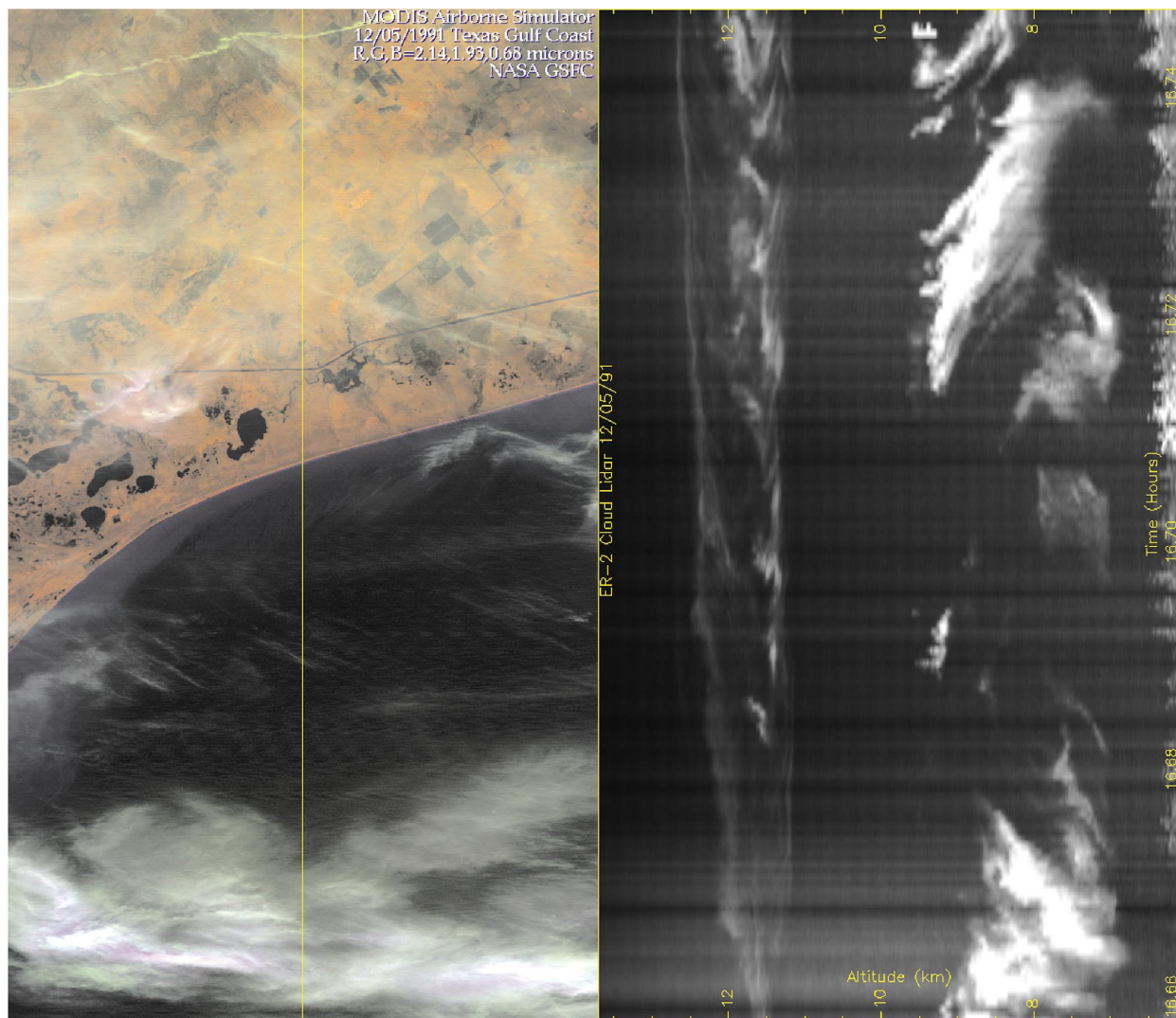
FIG. 1. (a) Three-channel RGB composite image over the Gulf of Mexico and nearby coast of Texas acquired by the MAS during FIRE-91 cirrus IFO (5 December 1991); and (b) Lidar attenuated backscatter profile as a function of distance along the ER-2 ground track, along a line down the center of the MAS image (see text for details).

which to perform radiative transfer calculations. We will demonstrate that extremely inhomogeneous media are not required for there to be significant departures in the radiative properties of clouds from their plane-parallel counterparts.

3. Modeling approaches

In our previous study (Gabriel et al. 1993), we explored the effects of spatial variations in cloud optical properties on their bulk radiative properties using the Fourier–Riccati (herein referred to as FR) radiative transfer model. The FR model was also used to examine the importance of cloud sampling on the accuracy of calculated shortwave radiances and fluxes emerging at the cloud boundaries. This study extends

the aforementioned work by addressing the relative importance of cloud microphysics and cloud morphology on spectral reflectance as well as heating and cooling rate profiles of cloudy media.

a. Radiative transfer model

Here we briefly describe the FR model, leaving mathematical details to the appendix. The development of the model begins with the equation of radiative transfer for spatially inhomogeneous scattering and absorbing three-dimensional media. The radiances and phase function are expanded in terms of a sum of their respective azimuthal components. This results in a system of *coupled* integro–differential equations. The horizontal partial derivatives of the radiance field are trans-

formed to algebraic functions by taking their Fourier transform yielding a system of coupled ordinary 1D differential equations. In the absence of horizontal variability this yields the well-known *decoupled* system of 1D equations that describe radiative transport in plane-parallel media. While it is possible to solve the transformed equations by iterative methods commonly applied to the numerical solution of boundary value problems, advantages are gained if the boundary value problem is reformulated as an initial value problem. By applying the interaction principle, the resulting nonlinear system is solved for the response operators by a fourth order Runge–Kutta solver. The advantages realized are (i) the solver steps through the medium in either prescribed increments or variable step-sizes determined automatically that calculate the results to within a prescribed accuracy; (ii) the response operators, calculated only once, permit the rapid calculation of the radiances anywhere within the medium for an arbitrary number of sources with variable boundary conditions; and (iii) solutions are stable and accurate even under optically thick and highly inhomogeneous conditions.

The principal limitations of the FR method are determined by the size of the matrices and the number of matrix multiplications involved in the calculation of the radiative response operators. The size of the matrices is determined by the number of Fourier components required to represent the extinction and scattering functions and the number of terms in the Legendre series expansions of the anisotropic phase functions. To alleviate this problem an asymptotically fast matrix multiplication algorithm was used that for large matrices is of order $N^{2.8}$ complexity as opposed to N^3 characteristic of normal matrix multiplication. Thus, while the FR approach is computationally impractical on small workstations, it can be efficient when properly implemented on massively parallel computer systems where matrix multiplications are performed in parallel.

b. Atmospheric model

The calculation of the radiative properties of cirrus clouds is difficult since little is known about the spatial distribution of their optical properties. Geometrically complex ice crystals give rise to strongly anisotropic phase functions, while difficulties in obtaining accurate particle size distributions exacerbate uncertainties in their optical properties. The apparent radiative properties of clouds are also affected by the absorbing and emitting atmospheric gases (and to some extent the underlying surface). Thus, spectrally integrated, multidimensional radiation calculations directed toward understanding cloud energetics and remote sensing are not yet fully computationally feasible.

Confronted by the desire to understand how cloud reflectances and heating and cooling rate profiles are affected by variability in cloud optical properties, cou-

pled with the large number of unknown characteristics of this problem, it is necessary to simplify the radiative transfer simulations in a manner that is commensurate with the capabilities of our computational tools without grossly oversimplifying the problem. Thus, not only must the cloud be synthesized in a way that assists in the interpretation of the resulting radiation fields, but spectral bands must be selected wherein the radiative interactions of the cloud with the atmosphere and with the underlying surface are minimized. To make this problem tractable, we chose a commonly used tropical atmosphere model (McClatchey et al. 1972), within which a cirrus-like cloud was embedded. The cloud was located at an altitude between 10 and 14 km where the mean pressure and temperature were approximately 250 mb and 230 K, respectively. The lower boundary of the atmosphere was the tropical ocean, approximated by a nonreflecting surface whose temperature was fixed at 300 K. Finally, the solar zenith angle was selected to be 30°. For the purposes of radiative transfer calculations, the most important considerations involve the selection of microphysics, spectral bands, and cloud morphology. These are discussed below.

1) MICROPHYSICS

To retain features of measured particle sizes, we selected a distribution obtained from the FIRE-86 Cirrus IFO, as illustrated in Fig. 2a (Stackhouse and Stephens 1991). The distribution appears truncated below 25 μm because the instrument was incapable of detecting smaller ice particles. The dotted line shown is a possible, hypothesized extension of the measured size distribution. Such an extension allows for investigating the sensitivity of heating and cooling rates and the spectral reflectance to smaller particles. The added small particles constitute a fraction of about 20% of the total mass. While such a fraction could have been measured by other instruments (e.g., Arnott et al. 1994), it is nevertheless used here as an upper bound of uncertainty in the cloud microphysics, to be used in the sensitivity studies. In the investigations to follow we have referenced the measured size distribution as Case 1, while Case 2 refers to the inclusion of small particles.

To approximate the required cloud optical properties, we performed Mie calculations. The approach of equivalent surface-area spheres is adopted for the nonspherical ice particles in Mie calculations of the single-scattering albedo and volume extinction cross section. Figures 2b and 2c illustrate the spectral dependence of the single scattering albedo using the Case 1 and Case 2 size distributions. In the near-infrared region, the inclusion of small particles causes the single-scattering albedo to exceed that calculated from the measured particle sizes. In the greater part of the window region, this tendency is reversed. The effect of adding small particles increases the volume extinction cross section, hence increasing the optical depth. This increase
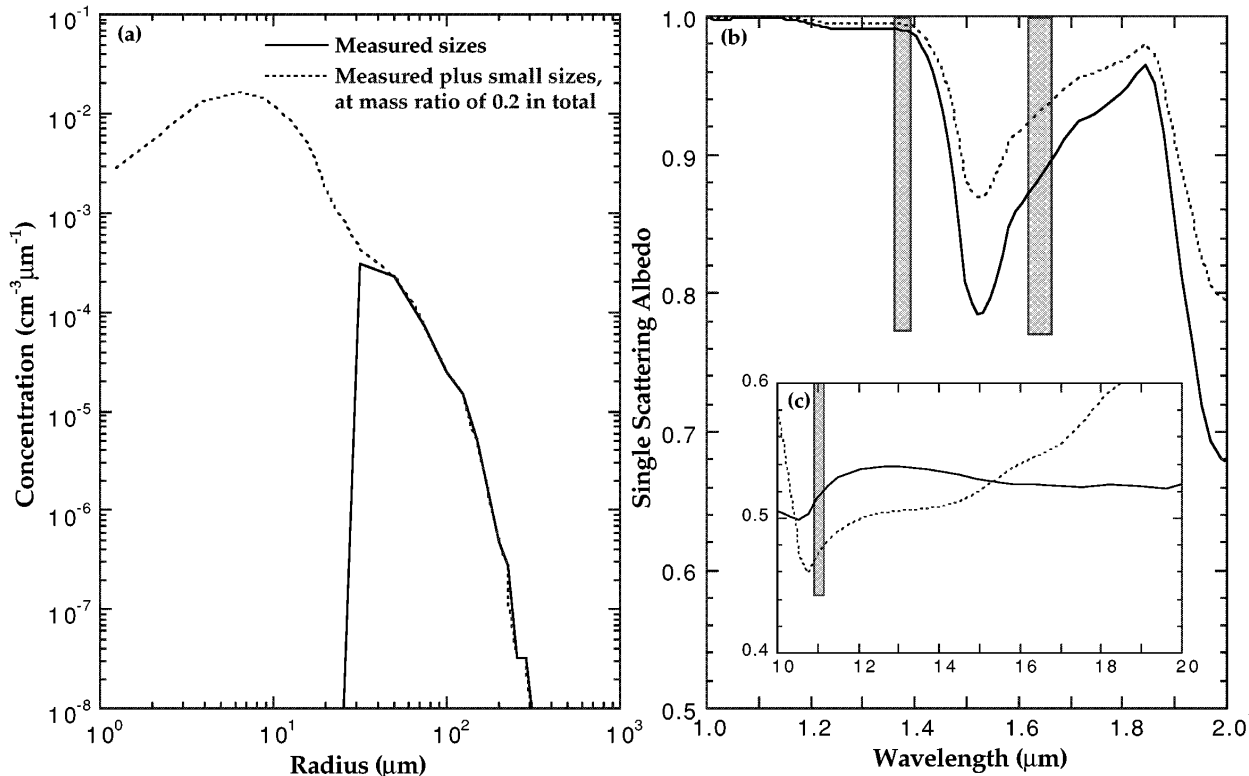
FIG. 2. (a) A measured particle size distribution (mass m, solid line truncated at 25 μm) acquired during FIRE-86 cirrus IFO, and the corresponding size distribution obtained by adding small particles (mass f, dotted line), constituting a fraction of 20% [$f/(m + f)$] of the total mass; (b) Mie calculations with equivalent area spheres of the single scattering albedo from both size distributions in (a) in the near-infrared regions (shaded area for the 1.38-μm and 1.64-μm spectral bands); and (c) as in (b), but for the infrared regions with 11-μm spectral band shaded.

amounts to a factor of nearly 2 for a 20% increase in the mass due to the addition of small particles.

In the FR model, the phase function must be expanded in a Legendre series. Phase functions calculated from simple ice crystal forms (e.g., sphere, plate, column, etc.) are either extremely anisotropic or exhibit many features. These require a large number of terms in their expansion that precludes their usage in the radiation model. Instead, the Henyey–Greenstein phase function is often used in radiative transfer models. The attraction of this phase function lies in its mathematical simplicity: being the generating function of Legendre polynomials, the coefficients involved in its expansion are powers of the asymmetry parameter (or the first moment). Although Henyey–Greenstein phase functions cannot reproduce any realistic phase function (except for isotropic), they are good approximations for flux calculations since the first moment is the dominant term. To model radiance fields accurately, however, detailed features (i.e., higher-order moments) of the phase function are important (cf. King 1987).

Recently, Takano and Liou (1995) performed theoretical calculations of the phase function for a single ice crystal using a detailed ray-tracing technique. Two phase functions in the 1.38-μm band corresponding to solid and hollow ice crystals are illustrated in Fig. 3. The phase function associated with the solid columns has many complex features including strong backscattering. The one for hollow columns reveals smoother features and can be crudely represented by the Henyey–Greenstein phase function having an asymmetry parameter equal to 0.7. In addition, Stephens et al. (1990) argued that results derived using a Henyey–Greenstein phase function with $g = 0.7$ are in better agreement with aircraft data collected during FIRE-86 cirrus IFO. To obtain accurate monochromatic radiances in FR simulations, even with a Henyey–Greenstein phase function, requires nearly 3 CPU hours of a Cray-YMP supercomputer. Since hollow ice columns are often found in cirrus clouds and faced with limited computing resources, a Henyey–Greenstein phase function with $g = 0.7$ was used for all spectral calculations.

2) SPECTRAL SELECTION

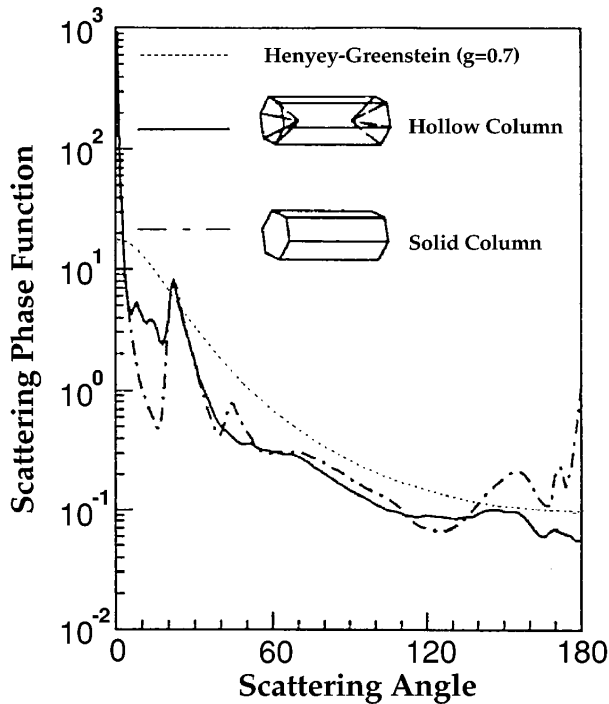Absorbing and emitting gases in the atmosphere greatly escalate the computational cost and complexity

FIG. 3. Ice crystal scattering phase function for hexagonal solid (dot–dashed line) and hollow (solid line) columns in the 1.38-μm band, together with a Henyey–Greenstein ($g = 0.7$) phase function (modified from Takano and Liou 1995).

of multidimensional radiative transfer calculations on account of their wildly varying spectral characteristics. Correlated k-distribution methods (e.g., Goody et al. 1989) are useful for treating the nongray, inhomogeneous atmospheres. Gaseous absorption can be formulated into a matrix form whose elements depend on the absorption strength, proportion of gas, and the thermodynamic state of the atmosphere. While this approach can be readily incorporated with molecular and particulate scattering, it increases the computational burden dramatically. Complexity is increased further when the spectrally dependent bidirectional properties of the surface must be considered. Clearly a compromise must be reached. Given that our resources are limited, we believe that the best that we can achieve is to select a few spectral bands whose characteristics allow for the attainment of the goals of this study. We have chosen three bands centered on 1.38 μm, 1.64 μm, and 11 μm for exploring remote sensing and atmospheric energetics issues.

There are many spectral bands suitable for the remote sensing of cirrus clouds. These bands can be used either in combination or individually. In the solar portion of the spectrum, atmospheric gases produce at least four strong absorption bands centered at 1.38 μm, 1.88 μm, 2.7 μm, and 3.2 μm. Of these, the first one is due solely to water vapor; the rest suffer from additional

contamination from either carbon dioxide or ozone. (Note that only the 1.88-μm and 3.2-μm bands are included in the MAS.) These bands effectively decouple the reflected radiances of cirrus from those of the surface, minimizing the complications introduced by surface reflection (e.g., Barton 1983; Gao et al. 1993). The vertical distribution of cirrus, water vapor, carbon dioxide, and ozone are quite different. This helps in some ways to simplify the radiative transfer problem.

To characterize the radiative properties of cirrus by remote-sensing techniques, the 1.38-μm band (1.36–1.39 μm, one of the MODIS channels) is the best choice for the following reasons: in most cases, cirrus clouds are in the upper troposphere above the bulk of atmospheric water vapor. For the tropical atmosphere, considered in this study, the fraction of the direct solar radiation reaching cloud top is about 99%. Very little direct or diffuse radiation is reflected back to the cloud base from the surface. Hence, only small corrections need be made if assuming no diffuse radiation enters the boundaries of the FR model. Ice particles absorb solar radiation in increasing amounts from 1.38 to 3.2 μm (single scattering albedo decreases from ~0.99 to 0.56). This rapid variation in absorption complicates the interpretation of remotely sensed data. At longer wavelengths, the amount of incoming solar radiation diminishes sharply. For example, in the 1.88- (or 3.2-) μm band, there is nearly a three (or twenty) fold reduction in solar energy, compared to the 1.38-μm band, in terms of which the signal to noise ratio deteriorates greatly. Based on the aforementioned reasons, we chose the 1.38-μm band to study the reflected signature from cirrus clouds. For the radiative transfer calculations, the amount of solar radiation reaching cloud top was first modified to account for the intervening atmosphere. Transmission of radiation from the top of the atmosphere to cloud top and back to space was computed at 10 cm^{-1} resolution. The optical properties of cirrus were further divided into three subbands since they vary relatively smoothly (as shown in Fig. 2b).

For the purpose of determining the radiative heating and cooling rate profiles of cirrus, spectral integrations were necessary. Again, this is computationally burdensome for multidimensional radiation simulations due to the presence of absorbing gases. An effective way of reducing the difficulties introduced by absorbing gases is to use those atmospheric windows that also contain the representative absorption and emission signatures of cirrus clouds. The validity of narrow- to broadband conversion (or some types of weighting) schemes, while of concern here, falls outside the scope of this paper and is properly the subject of further research.

Of all the window channels in the solar spectral region, the 1.64-μm band (1.62–1.66 μm, one of the MODIS channels) is attractive because the intervening atmosphere between the cloud and the surface is transparent, whereas ice particles exhibit strong absorption. At this wavelength, the emission of surface radiation is

negligible in comparison to the solar contribution that is about 9.2 W m^{-2} reaching cloud top (less than 0.2% depression). The reflectance by the ocean is generally negligible at 1.64 μm, except for sun glint regions that could provide extra solar radiation for cloud heating. Finally, the 11-μm band was selected because, as shown in Fig. 2c, it is an atmospheric window where thermal radiation is the dominant source and cirrus clouds are strongly absorbing. Since the thermal radiation produced from the average temperature between surface and cloud is about 25% of the total solar radiation, we limited the bandwidth to 0.1 μm to balance the heating contribution from the 1.64-μm band. This 11-μm band is also one of the MODIS channels but about five times narrower. In the following radiation simulation, the cloud optical properties in these two bands are also divided into three subbands.

3) MORPHOLOGY

The spatial distribution of the optical properties of naturally occurring clouds is extremely variable as is well known. Geometric forms such as cubes, cylinders, etc., possess internal uniformity in their optical properties and are frequently used for defining cloudy media in radiative transfer calculations. However, clouds are internally inhomogeneous and, in general, so variable that even their external appearance cannot be described by highly idealized geometry. Qualitatively, clouds are perhaps more accurately described by their morphology, a word that suggests amorphous textures consistent with our perception of clouds. Quantitatively, morphology is specified by the spatial distribution of cloud extinction and scattering densities and phase functions.

Although there have been several studies that describe the composition of cirrus, few theoretical or observational studies appear to have been undertaken to address their morphology. It is certain that radiative transfer will be affected by cloud morphology, but to what extent the apparent radiative properties are sensitive to inhomogeneity in the optical properties is as yet not well understood. To explore these issues, we elected to use simple Gaussian-shaped extinction and scattering densities that only exhibit horizontal variability while fixing the phase function. Certainly far more complex morphologies could have been used, but this relatively simple one assists the intuition in establishing a connection between cloud structure and the simulated radiation fields that might be obscured by more complex cloud morphologies.

The extinction density used as an input to the FR model has a spatial dependence given by $\alpha(x) = 4 \exp(-\pi x^2)$. The scattering density is linearly related to the extinction density through the single scattering albedo. The appearance of this cloud, as illustrated in Fig. 4, may be described best as a translucent mass bounded by two plates with a high extinction density near its center, becoming very tenuous toward its edges. This cloud is periodic (e.g., cloud street) as required by the boundary conditions of the FR model. The extinction density was truncated at the horizontal coordinates X = ± 2 where it attains a very small value ($\sim 10^{-6}$). Thus, an individual cloud cell has an aspect ratio of 4:1, extends horizontally to 16 km, and is 4 km thick. The domain-averaged extinction density is unity with a standard deviation of 1.35. To quantify roughly the variability of this cloud, we calculated the coefficient of variation. For a given field, this coefficient is defined as the ratio of the standard deviation to the mean of a field. For this cloud, the coefficient of variation of the extinction density is 1.35.

4. Results

Two major problems of radiative transfer are remote sensing and the determination of heating and cooling rates in clouds. Here we attempt to illustrate the relative roles of microphysics and morphology on the radiative transfer and consider the aforementioned problems in this choice.

a. Applications to remote sensing

Interpretation of any radiance data in terms of cloud properties requires the use of a forward radiative transfer model. These models are necessarily simple and based on 1D radiative transfer theory. Unfortunately, this simple depiction of radiative transfer introduces errors, and, while we do not intend on quantifying these errors in detail here, we aim to illustrate their nature as introduced by effects of cloud morphology. Our focus here is on the 1.38-μm radiances. Figure 5a shows the radiance field in the 1.38-μm band derived from the measured particle size distribution (Case 1) for the Gaussian cloud already discussed. The plot can be considered as an image viewed by a satellite traveling and scanning along the x-axis (alongtrack image, cf. Fig. 4). The solar zenith angle is 30° with the sun located on the right-hand side of the figure. The viewing angle is defined as positive if the satellite sensor views toward the sun and is negative when measuring backscattered sunlight.

The simulated radiance field exhibits a large variability. Although not shown, a plane-parallel cloud having both identical microphysics and a mean optical depth equal to that of its inhomogeneous counterpart would generate vertically banded radiance fields (viewing angle versus horizontal location, as in Fig. 5a). Thus, differences between 2D and plane-parallel (P-P) clouds are profound. Figure 5b shows the image produced by the independent pixel approximation (IPA) using identical inputs as in the 2D case. The IPA performs independent plane-parallel computations using the local optical properties of the extinction field. This figure shows that the angular distribution of the radiance field is symmetrical about the cloud center since
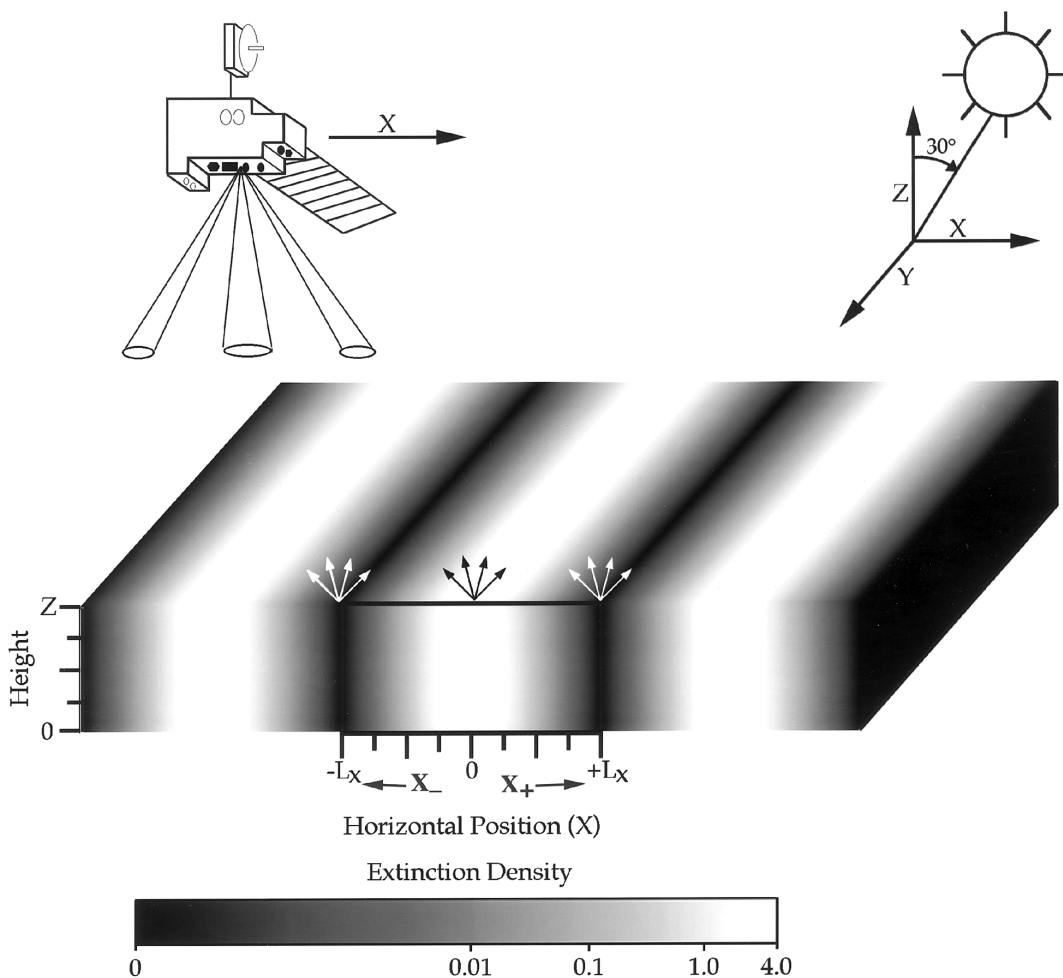
FIG. 4. Gaussian extinction density function with a domain average of unity. This cloud is periodic with a wavelength of $2L_X$ and vertically constant. Practically the extinction density can be truncated at the horizontal coordinates $X = \pm 2$ and yields an aspect ratio of 4:1.

the cloud is symmetrical. Comparison between Figs. 5a and 5b highlights the fundamental role of lateral photon transport.

To further explore the subtle differences between radiances computed from 2D and P-P radiative transport, it is appropriate to consider the radiance field at optical depths equivalent to the domain-averaged value (i.e., $\tau = 1$). These coordinates are designated as X_+ ($\tau = 1$) on the right-hand plane; X_- ($\tau = 1$) on the left. Figure 6 shows the angular distribution in the principal plane. Beginning with the P-P case (solid curve), it is seen that the radiance field is smooth with two peaks near the horizon and a slight depression at nadir. This pattern of reflected radiances is identical to that of the IPA. The radiances do not exhibit any undulations (e.g., the glory) because the Henyey–Greenstein phase function is monotonically decreasing, possessing a forward peak at the origin (cf. Fig. 3) and no backscatter peak. The phenomenon of limb brightening gives rise

to peaks in the reflected radiance distribution near the horizon.

In the 2D cloud, the situation is more complex because of the effects of inhomogeneity. With respect to X_+ and X_-, it is expected that the reflected radiance is not symmetrical, even though the cloud extinction is symmetrical. The only possibility of observing symmetrical radiances would be for overhead illumination. The directional preference of the incident photons is responsible for the skewness of the observed radiance field (cf. Fig. 5a). To the right of X_+ (e.g., Fig. 4), the cloud is tenuous; to the left, the optical density increases until the center of the cloud is reached. Photons entering near X_+ will continue their trajectory to the left where they will experience increased multiple scatterings. If in the process of scattering they enter to the right of X_+, they will encounter fewer cloud particles and hence have a high probability of escaping. Consequently when viewing toward the sun side (i.e., pos-
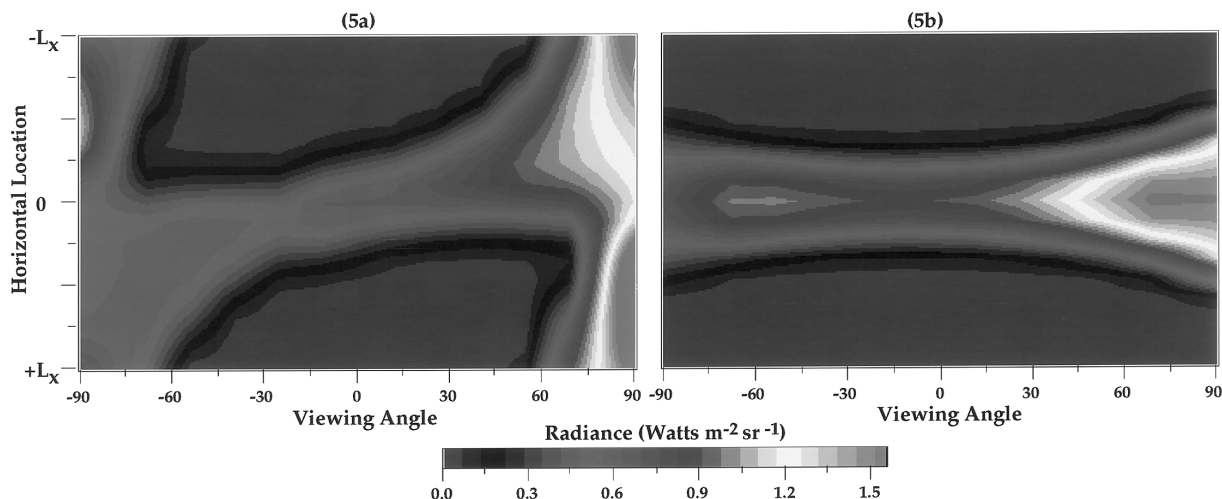
FIG. 5. Spatial and angular distributions of reflected radiances integrated over the 1.38-μm band ($\Delta\lambda = 0.03$ μm), using the measured size distribution (Case 1 in Fig. 2a) and the Gaussian cloud (shown in Fig. 4) for (a) 2D and (b) IPA simulations. The sun is located on the right-hand side of the figure with 30° zenith and 0° azimuth angles. The viewing angle is positive toward the sun side and negative otherwise.

itive angles, solid triangles in Fig. 6a), darkness will prevail until grazing angles are reached, whereupon scattering by the adjacent cloud becomes dominant. In contrast, viewing away from the sun, photons moving to the left of X_+ will undergo numerous scatterings and hence have a greater chance of exiting by backscattering. Thus, the slowly varying P-P radiance field between $-50°$ and $50°$ is in marked contrast to that of the 2D pattern. In addition, the position of the backscattered peak of the 2D cloud is quite different from that of the P-P cloud. These effects are caused by the presence of inhomogeneity.

To the right of X_- the extinction density increases; to the left, the cloud becomes increasingly tenuous. This situation is exactly the opposite of that near X_+. Thus, viewing toward the sun side at X_-, the increase in the number of multiply scattered photons causes the radiance to attain large values. Viewing away from the sun, on the other hand, the extinction density diminishes; hence the magnitude of the radiance will be even less than that at X_+. The radiance fields for the $X_\pm$ pair intersect near nadir. At this viewing angle, disparities between the radiances calculated for the 2D and P-P clouds are minimized. This is attributable to the total photon pathlengths being most comparable. Caution should be exercised in the interpretation of radiances departing from nadir since differences from P-P can be very large, often exceeding 50%. Although it is not possible to generalize from this study a viewing strategy for the purposes of remote sensing applications that minimizes the effects of inhomogeneity, our results lend support to the notion that the optimal viewing direction, for the purpose of minimizing the effects of cloud inhomogeneity, is near nadir.

Our discussion thus far has been focused on the effects exerted by the variability in the cloud extinction density on the radiance fields. To describe the influence of microphysics on the reflected radiances, Fig. 6b shows radiance distributions when small particles are included in the Mie calculation of the single-scattering albedo. The effects of the latter were isolated from other factors by fixing the extinction density as in Case 1. By comparison to Fig. 6a, it is clear that small particles do not affect the radiance distributions significantly. However, in Fig. 6c, when the effect of mass loading due to the inclusion of small particles is included, the extinction density is nearly doubled. This causes the P-P and 2D radiances to increase almost twofold. That cloud microphysics affects the magnitude of the radiance distribution is expected in as much as the inclusion of more particles changes the amplitude of the extinction density. Of greater importance is that for a given microphysics, morphology affects the radiance distribution in a more complex manner. This makes difficult the task of predicting with confidence the distribution of reflected radiances, hence compromising the accuracy of cloud retrievals of optical thickness and effective radius (e.g., Nakajima and King 1990).

To mitigate the effects of cloud inhomogeneity, we degraded the 2D radiance fields by a simple linear average of the domain size (e.g., from 1 to 16 km resolution). Such a degradation is employed in many applications (e.g., climate studies) that require reflected radiances measured at one scale to be degraded to a coarser resolution. Figure 7 compares domain-averaged radiances obtained by 2D to those of IPA (open circles) and 2D to P-P (solid circles). To avoid unnec-
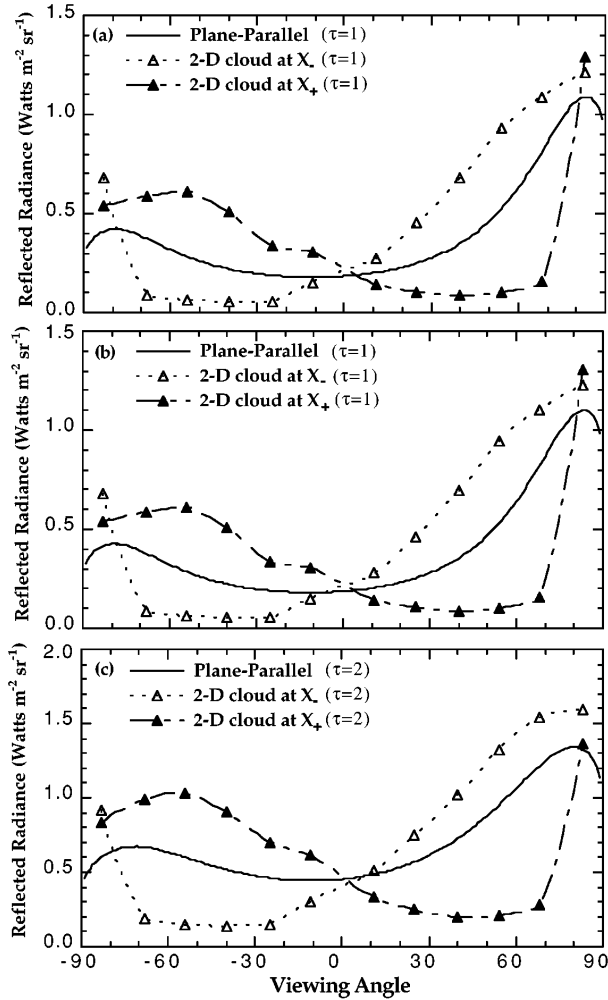
FIG. 6. Comparison of angular distributions of reflected radiances, integrated over the 1.38-μm band, where (a) assumes the measured size distribution and $\tau = 1$, (b) as in (a) except that small particles are included, and (c) as in (b) except $\tau = 2$ (see text for details).

viewing angles than 2D. This good agreement of the means may well depend on the choice of cloud morphology. This points to the need for more sensitivity studies.

b. Applications to radiative heating and cooling

The absorption and emission of radiation by clouds give rise to a radiative heating or cooling that can modulate life cycles of clouds (e.g., Webster and Stephens 1980). The conventional calculation of spectral heating and cooling rates in cloudy media can be expressed as

$$\frac{dT}{dt} = \frac{-1}{\rho C_p} \nabla \cdot \mathbf{F}_\lambda, \tag{1}$$

where ρ is the density of dry air, C_p its heat capacity at constant pressure, and $\mathbf{F}_\lambda$ the spectral net radiative flux. If the cloudy volume consists of internal thermal radiation sources {given by $B_\lambda[T(\mathbf{r})]$} and is illuminated by direct solar radiation (πF_0), the net flux divergence is given by (refer to the appendix for details)

$$-\nabla \cdot \mathbf{F}_\lambda = k_\lambda(\mathbf{r})\{4\pi \bar{I}_\lambda(\mathbf{r})$$
$$+ F_0 \pi \mu_0 \exp(-\tau_\lambda(\mathbf{r})) - 4\pi B_\lambda[T(\mathbf{r})]\}, \tag{2}$$

where the direct solar radiation is incident at an angle $\theta_0 = \cos^{-1}\mu_0$ with respect to the vertical axis. The slant optical depth $\tau_\lambda(\mathbf{r})$ is calculated from the source to position $\mathbf{r}$ in a direction given by θ_0. The quantity $\bar{I}_\lambda(\mathbf{r})$ is the radiance integrated over all solid angles, also called the mean intensity. Finally, the spectral absorption density is given by $k_\lambda(\mathbf{r})$.
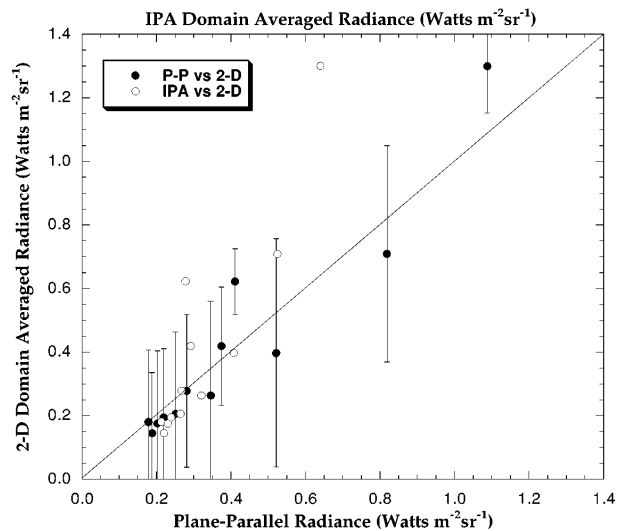
essary cluttering of the figure, only the standard deviations for the latter case are shown. The large standard deviations suggest that the underlying cloud variability is significant. While the coefficient of variation of the cloud (i.e., that of the extinction density) is 1.35, the largest value for the domain-averaged radiances is 1.30. This supports the idea stated in Part I that radiative transfer acts as a smoothing operation, filtering out small-scale cloud inhomogeneity. In the case of IPA, the coefficient of variation for the radiance field can exceed that of the cloud because the smoothing action induced by lateral photon propagation is inhibited. In the P-P case, the angular distribution of radiances was obtained by employing the mean optical depth ($\tau = 1$) of the 2D cloud. Although the domain-averaged radiances are in good agreement with one another, those of IPA or P-P tend to produce brighter reflectances at most

FIG. 7. Scatterplot of angular distribution of reflected radiances averaged over the domain for 2D, IPA, and P-P clouds in the 1.38-μm band. The open circles represent 2D versus IPA and solid circles for 2D versus P-P. To avoid unnecessary cluttering of the figure, only the standard deviations (vertical bars) for the latter case are shown.

Current practice of determining cloud heating and cooling rates is first to obtain the net fluxes above and below clouds and then to take the net flux divergence [Eq. (1)]. Potential sources of error in such procedures are numerous (e.g., Hayasaka et al. 1995) and some methods to correct for effects of side transport creating spurious absorption have been developed (e.g., Ackerman and Cox 1980). These drawbacks can be eliminated in principle by attempting to deduce absorption on the local level as implied by Eq. (2). In practice, the only difficulty—that of measuring the spectral absorption density—might limit the applicability of this technique. The strengths and limitations of the two methods are summarized in Table 1.

For the 1.64-μm and 11-μm wavelengths studied in this paper, we consider that the absorption occurs only by particles. Figures 8a and 8b show the solar heating in the 1.64-μm band and longwave cooling in the 11-μm band, respectively, for Case 1 microphysics and morphology. The spatial distribution of cloud heating in Fig. 8a is as expected: the greatest heating occurs near the upper boundary of the cloud that is exposed to the sun. The least amount of heating occurs near the lower boundary that is shielded from the sun by the intervening cloud or in that part of the cloud where the extinction density is tenuous. The heating rates are not symmetrical because the illumination is oblique.

The spatial distribution of the thermal cooling differs from solar heating since thermal emission is isotropic. The symmetry of the cloud therefore imparts symmetry to the cooling. However, the cloud is isothermal ($T_c = 230$ K) and is heated by its lower boundary ($T_b = 300$ K). Most of the cloud volume is heated by this large temperature gradient except for the small portion near the center at cloud top. This region, although optically sufficiently thick to shield itself from being heated from below, continues to cool radiatively into space. In contrast to Fig. 8, a P-P cloud having identical microphysics and a domain-averaged extinction density as in the 2D case would produce a heating or cooling distribution consisting of uniform horizontal bands. Symmetrical heating and cooling fields with magnitudes differing from Fig. 8 would be calculated by IPA using inputs as in the 2D case. Thus, IPA is expected to be more accurate than P-P.

To explore the competition between microphysics and morphology in establishing cloud heating and cooling rate profiles in more detail, the two locations used in the analysis of the radiance fields (i.e., $X_\pm$) were selected. Figure 9a shows the heating rate profiles for 2D and P-P (or IPA) clouds. The main features in Fig. 9a, the disparities in the heating rates between P-P and 2D clouds, are the result of horizontal heating gradients. These gradients are produced by absorption related to lateral photon transport across regions of varying extinction density. The IPA will also exhibit horizontal variation in the cloud heating, but this variation would be due to the radiative transfer occurring locally without lateral photon propagation.

In Fig. 9a, at cloud top the 2D heating rate profiles at $X_\pm$ are greater than that of P-P clouds. While at X_+ the profile is always greater than that of P-P, that at X_- changes significantly as cloud base is approached. The illumination by the direct solar radiation is uniform at cloud top, therefore the major contribution to the cloud heating will be the mean intensity described by Eq. (2). In the 1.64-μm band, the downwelling diffuse radiation at the upper boundary of the cloud is small enough to be excluded from further consideration. With reference to Fig. 6a, the hemispherical upwelling radiance is the only contributor to the mean intensity. Performing a simple integration, we find that the mean intensity at X_+ is the largest, followed by that at X_-, which in turn exceeds that of P-P. This analysis describes the magnitude of heating at cloud top as shown in Fig. 9a. Entering deeply within the cloud, the heating rate profiles are established by the joint contributions of two complex processes. These are the depletion of direct solar radiation and the corresponding increase of diffuse radiation as a result of this depletion (multiple scattering).

These processes are easier to understand near cloud base. First, the rate of depletion of direct radiation is greater at X_- than at X_+ because incoming photons must traverse longer paths through a higher-absorption density before they reach cloud base. Meanwhile, the rate of generation of diffuse radiation increases. Paralleling the argument at cloud top, the hemispherical downwelling radiance now becomes the sole contributor to the mean intensity. At X_+, the direct radiation

TABLE 1. Comparisons of the merits in determining atmospheric heating and cooling derived by flux divergence and mean intensity methods.

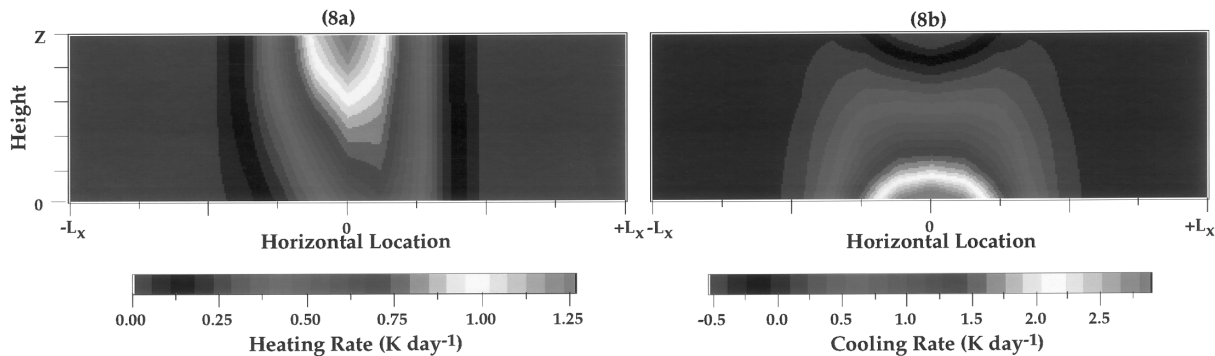|	Mean intensity		Flux divergence	
	Strength	Shortcoming	Strength	Shortcoming
Platform	Single	None	None	Collocation for double Stationarity for single
Aerodynamic	Simple	None	None	Attitude control
Energy	Addition	Need absorption coefficient	Embedded absorption	Subtraction

FIG. 8. Spatial distributions of (a) solar heating rate profiles in the 1.64-μm band for the measured particle size distribution (Case 1 in Fig. 2a), and (b) as in (a) but for thermal cooling rate profiles in the 11-μm band (positive for heating).

is generally greater than that of P–P since it suffers less attenuation. However, the P–P mean intensity is comparable to or larger than that near X_+. Therefore, the heating rate, being the sum of these two quantities, is larger at X_+ than that of P–P. In contrast at X_-, the rate of depletion of the direct radiation is very large by comparison to that of P–P. The rate of increase of the mean intensity at X_- is larger than that of P–P but cannot compensate for the greater depletion rate of the direct

radiation. The end result of this is that the heating rate is least at X_-.

Until now, our discussion has been focused on the manner by which heating rates are affected by cloud morphology. The influence of microphysics on cloud heating rate profiles are discussed below. Figures 9b and 9c show the heating rate profiles when the effects of small particles are included in the Mie calculation of the single scattering albedo in the 1.64-μm band. The
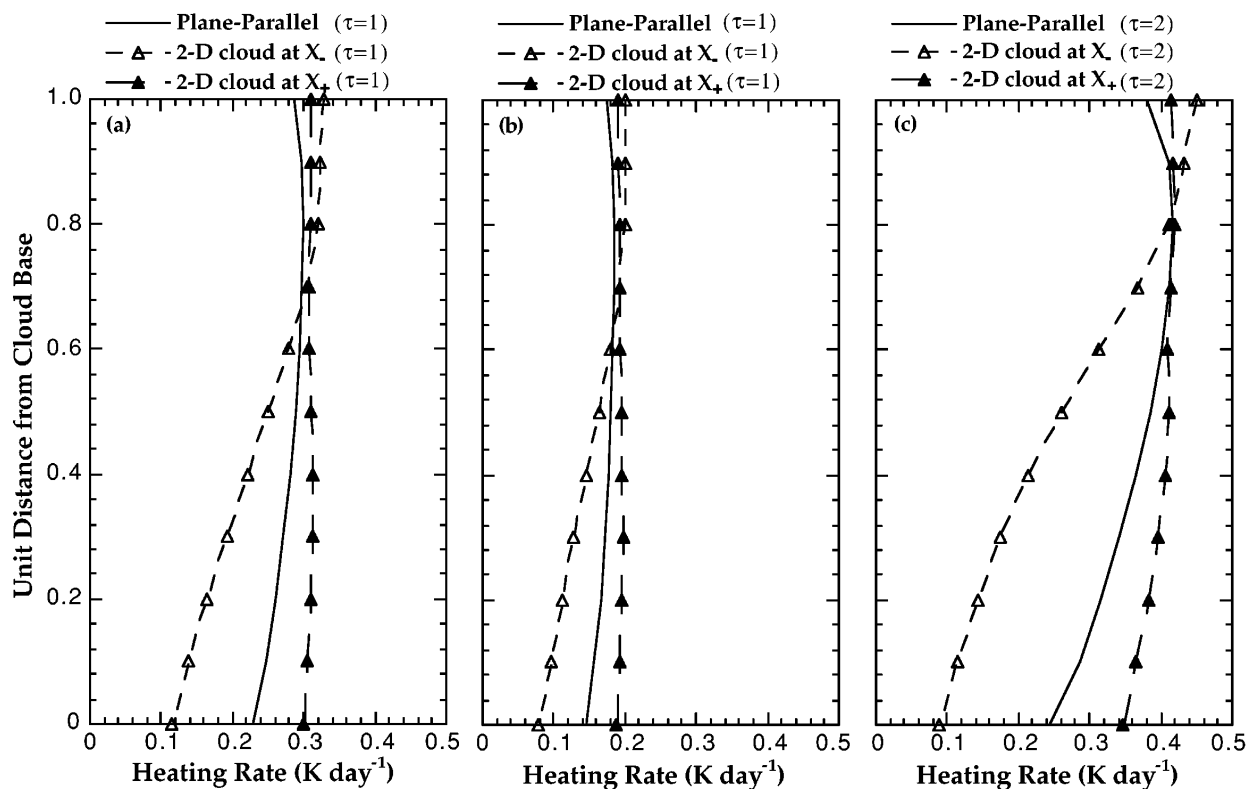

FIG. 9. Comparison of spatial solar heating rate profiles in the 1.64-μm band, where (a) assumes the measured particle size distribution and $\tau = 1$, (b) as in (a) except that small particles are included, and (c) as in (b) except $\tau = 2$ (see text for details).

inclusion of small particles increases the single-scattering albedo. By fixing the extinction density as in Case 1, the effects of the latter were isolated from other factors. In Fig. 9b the shape of the heating rate profiles is not altered by the inclusion of small particles. However, the amplitudes of the cloud heating rates are reduced significantly (more than 30%) because the increase in single scattering albedo reduces the absorption. Consequently, photons can penetrate deeper into the cloud as seen by the lowering of the intersection of the heating rate profiles at $X_{\pm}$.

When the effect of mass loading due to the inclusion of small particles is also considered, Fig. 9c shows that both the shape and magnitudes of the heating rate profiles are altered in comparison to Fig. 9a. Mass loading increases the extinction density nearly twofold. The intersection of the heating rate profiles at $X_{\pm}$ is elevated relative to that in Fig. 9a, even though photons can penetrate deeper into the cloud. The position of this intersection point is largely determined by the rate of attenuation of direct solar radiation. With reference to Eq. (2), the contribution from direct radiation depends on the weakly varying absorption and exponentially decreasing slant optical depth. Thus, the depletion rate of direct radiation exceeds that of Fig. 9a, elevating the intersection point.

Returning to the detailed analyses of the cooling rate profiles in the 11-μm band, Fig. 10 shows three plots calculated using the same procedures described in the heating rate calculations. Figure 10a illustrates the cooling rate profiles for 2D and P-P (or IPA) clouds using the measured microphysics. The symmetry of the 2D cloud cooling rate profile at $X_{\pm}$ has already been discussed. From Eq. (2), and suppressing the direct radiation, cloud cooling is proportional to the difference between the mean intensity and the Planck function. Since the cloud is isothermal, the Planck function within the cloud is constant. Near cloud base, there is strong heating from the lower (warmer) surface. The difference in cooling rate profiles between the P-P and 2D cloud is attributed to horizontal inhomogeneity. The latter causes the 2D cloud near $X_{\pm}$ to appear less opaque than its P-P counterpart. Hence, this provides more thermal radiation from the warmer lower boundary to be absorbed by the 2D cloud than its P-P equivalent.

The cooling rate profiles in Fig. 10b are similar to those in Fig. 10a, while disparities in their magnitudes are accentuated. The inclusion of small particles increases the absorption (cf. Fig. 2c), which is the main cause of these disparities. Finally, the inclusion of mass loading enhances the absorption as shown in Fig. 10c.
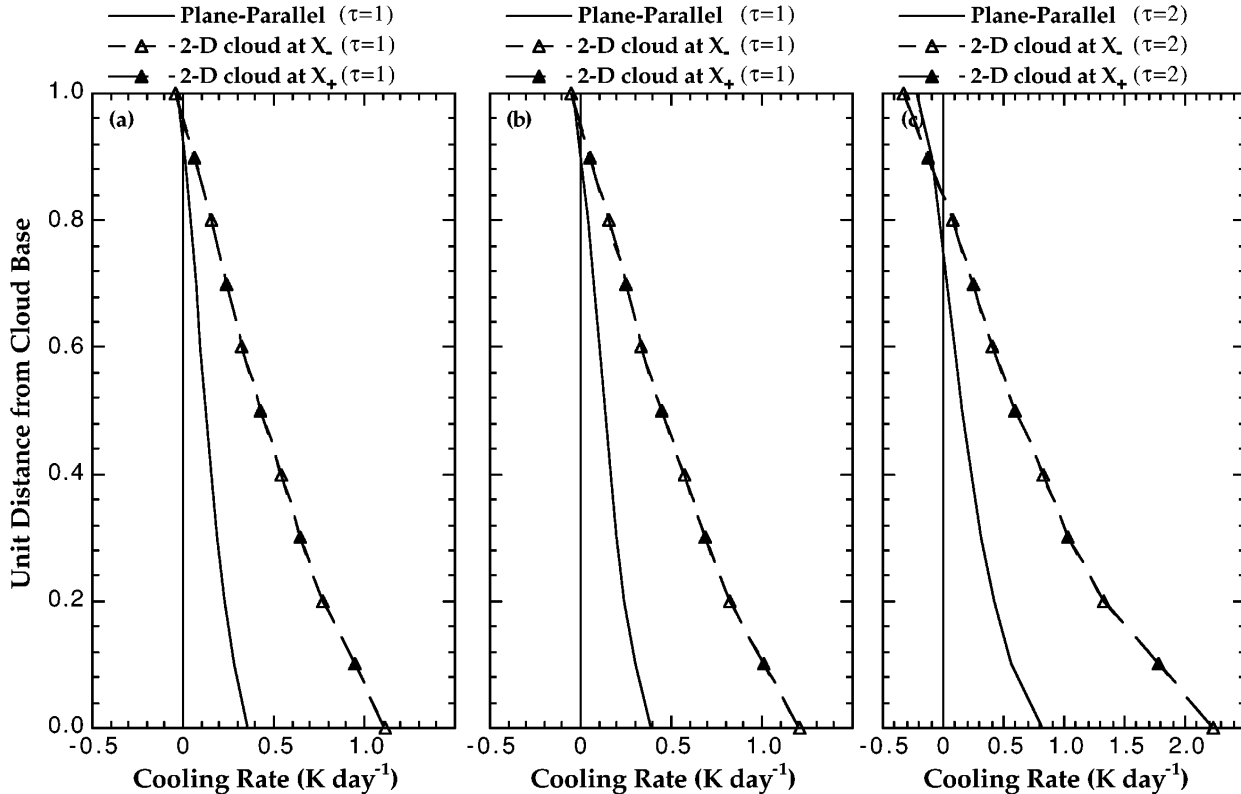

FIG. 10. As in Fig. 9 except for thermal cooling rate profiles in the 11-μm band (positive for heating).

The attendant increase in the extinction density prevents the cloud from being heated by the lower boundary, resulting in a larger cloud volume cooling to space. The insights we have gained from these analyses suggest that horizontal and vertical distributions of heating and cooling rates can be affected significantly by the presence of cloud inhomogeneity. The horizontal variation of 2D cloud heating and cooling rates can cause a radiatively induced secondary circulation that modifies directly the local production and destruction of vorticity and kinetic energy through buoyancy forces (Starr and Cox 1985). This effect cannot be observed in P-P clouds because of the absence of horizontal gradients in its radiative properties.

Figure 11 shows a comparison of the domain-averaged, spectral heating rates at 1.64 μm (solid circles) and cooling rates at 11 μm (open circles) at various levels inside the 2D and P-P clouds. In this study, trends in the solar heating and thermal cooling rates appear reversed. Relative to the 2D cloud, P-P overestimates solar heating and underestimates thermal cooling. Previous studies (e.g., Harshvardan and Weinman 1982; Stephens and Preisendorfer 1984) illustrated the importance of the exchange of radiative energy through the sides of finite clouds. While well delineated cloud edges are not possible to define in the 2D cloud (cf. Fig. 4), nevertheless, the extinction is significant in less than one-half of the domain. The observed trend reversal is caused by the fundamental differences between the solar and thermal sources, finite cloud effects, and the influence of boundary conditions on the radiative transfer. When a collimated beam of photons impinge on a cloud boundary, the strongly forward-scattering phase function increases the possibility of photons to traverse the cloud and exit its sides. This results in fewer absorptions and hence a reduction in heating relative to the P-P cloud. In the case of thermal emission, the boundary conditions play a crucial role since now the cloud sides can absorb photons originating from the lower boundary from all directions. This situation has no plane-parallel analog.

The problem of how the radiative transfer is affected by finite clouds is subsumed by the more general problem of how the scale dependence in cloud inhomogeneity affects its radiative properties. One important example is the requirement to calculate the flux divergence averaged over some scale. Thus, the issue of how well an inhomogeneous cloud (e.g., a cloud with a variable extinction) can be approximated by a plane-parallel medium requires an understanding of how the scale dependence of the inhomogeneity affects the photon pathlength distribution. The latter must surely be dependent on statistical properties of cloud morphology and is the subject of ongoing studies.

5. Summary and conclusions

Within the last decade, many large field experiments have been conducted in an effort to characterize and
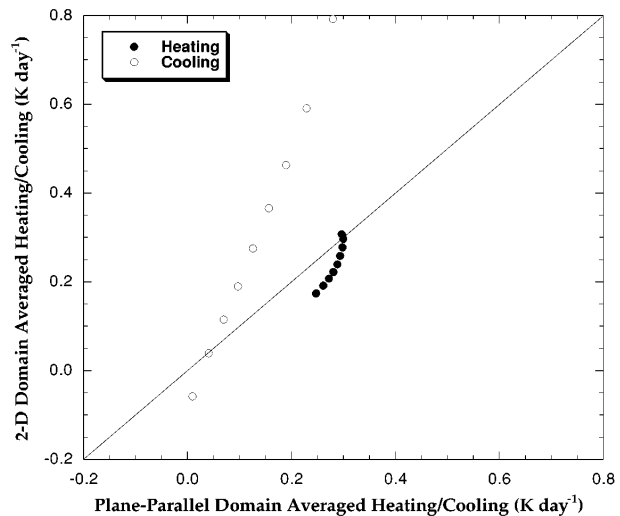

FIG. 11. Scatterplot of heating and cooling rates averaged over the domain for 2D and P-P clouds in the 1.64- and 11-μm bands, respectively. The solid circles represent heating and open circles for cooling. To avoid unnecessary cluttering of the figure, the standard deviations are not shown.

understand the radiative and microphysical properties of cirrus. The motivation for this study derives from appreciating the large disagreements between in situ measurements of cloud properties (e.g., effective particle radius and optical depth) from the FIRE-86 IFO. Two size distributions were used to quantify the effects of microphysics on cloud radiative properties. The first employed measured particle size distributions from the 1986 IFO; the other artificially introduced smaller particles that were inferred but not detected. In addition, by examining various radiometric data obtained during the FIRE-91 IFO, the presence of large variability in the radiative signatures suggested that cloud morphology may play a significant role. The effects exerted by both microphysics and morphology on the radiative properties of clouds are the theme of this work.

To explore the issues highlighted above, we extended the capabilities of our Fourier–Riccati radiative transfer model to accommodate more general boundary conditions and internal sources. Unfortunately, a thorough investigation of cloud radiative properties is computationally prohibitive since microphysical, spectral, and spatial variability would have to be addressed. To achieve our objectives and yet still constrain the problem to manageable proportions, we determined that three spectral bands centered at 1.38 μm, 1.64 μm, and 11 μm would represent adequately the spectral regions of interest for studying remote sensing and energetics issues of cirrus-like clouds. Since many operational radiation models use plane-parallel or independent pixel approximations routinely, it is vital to examine the applicability of such techniques to inhomogeneous clouds. To assist in the understanding of the radiative

properties of nonuniform clouds, a spatially symmetric extinction density could provide cues for interpreting the radiative signatures. As a first step toward achieving this goal, a Gaussian extinction distribution was employed. Whereas in plane-parallel clouds there are no horizontal gradients in the extinction density, the Gaussian morphology used here is vertically uniform. This simplicity is designed to isolate the effects of horizontal inhomogeneity from other factors and at the same time gain insight into the effects of microphysics.

In summary, our analysis and interpretation of the calculated radiation fields connected with remote sensing and cloud energetics show that extreme inhomogeneity is not required to produce significant departure in the reflected radiance as compared to plane-parallel computations. The simple Gaussian morphology used in this study exhibits strong spatial variations of reflected radiances in the 1.38-μm band. This implies that cloud inhomogeneity can cause great difficulties in the quantitative usage of remotely sensed data. If a viewing strategy is required to suppress the effects of cloud inhomogeneity on the reflected radiance, this limited study suggests that a near-nadir viewing direction is optimal.

In the 1.38-μm band, cloud microphysics affects the magnitude of the reflected radiances in a systematic way since the inclusion of small particles in this study was observed to only alter the amplitude of the extinction density linearly. Cloud morphology affects the shape of the angular distribution of the reflected radiance in a more complex manner. From these limited observations, it seems that cloud morphology outweighs microphysics in determining reflected radiances from clouds. However, a more rigorous conclusion requires further research.

The degradation of the two-dimensional radiances by a simple linear average over the domain mitigates the effects of cloud morphology on the reflected radiances. Although the plane-parallel results and domain-averaged radiances obtained from independent pixel calculations are in good agreement with the degraded radiances of the two-dimensional cloud, the latter generally appear darker at commonly used viewing angles. This effect is inherent in multidimensional media and is due to lateral photon transport. The smoothing effect exerted by such transport was quantified by showing that the coefficient of variation of the cloud exceeds those of the reflected radiances. By comparison, the independent pixel approximation produced coefficients larger than that of the cloud (i.e., extinction density) since there is no possibility of horizontal photon transport in this approximation.

An alternative way of deriving atmospheric heating and cooling rate profiles is to use an approach based on measuring the mean intensity. This technique is generally superior to that of flux divergences, as shown in Table 1. The only requirement for its usage is knowledge of the absorption charac-

teristics of the medium. It is essential to the radiation community to develop practical ways of obtaining this fundamental quantity.

Cloud inhomogeneity affects the *local* heating and cooling rate profiles in the 1.64-μm and 11-μm bands, respectively. Local heating and cooling generate horizontal thermal gradients not observed in plane-parallel clouds and not correctly accounted for by the independent pixel approximation. These thermal gradients induced by radiation may be important contributors to the generation or maintenance of a secondary circulation in cirrus clouds. Relative to the domain-averaged two-dimensional heating and cooling rates, those calculated by plane-parallel theory showed a trend reversal, primarily because of the interplay between the source functions, boundary conditions, and finite cloud effects. Thus, caution in averaging cloud fields would have to be exercised since the localization of the heating and cooling may be an important mechanism for other physical processes.

The effects of cloud microphysics and morphology are similar to those discussed above in that the former dominates the magnitudes and the latter the shape of the profiles. The competition between diffuse and direct radiation sources is illustrated in the two-dimensional heating and cooling rate distributions. Differences between two-dimensional and plane-parallel results are partly due to shadowing of the direct solar radiation. This suggests that local heating in a multidimensional medium may be approximated by correcting for shadowing, hence modifying the source term in the independent pixel calculation. Since clouds do not possess a well-defined geometry, simple geometrical corrections for shadowing in plane-parallel calculations are difficult to apply. A statistical treatment of cloud inhomogeneity in radiative transfer calculations is more appropriate and requires further study.

Finally, the utility of combining a scanner for imaging with a lidar for profiling clouds is viable for indirectly studying cloud microphysics and morphology. Radiative transfer simulations can assist in the development of cues necessary for both subjective and possibly quantitative analyses of remotely sensed data. Thus, the interpretations of these signals requires an understanding of the sensitivity of multidimensional radiation to cloud variability. This paper provides a preliminary step toward this goal.

APPENDIX

Extension of the Fourier–Riccati Radiative Transfer Model

The Fourier–Riccati model developed in Part I was used to calculate spectral radiance and flux fields (the index λ will be suppressed) emerging at boundaries or within media that exhibit spatial inhomogeneity in their optical properties. To meet the requirements of this study, we extended this model to include thermal sources, emitting and reflecting boundary conditions, and the capability of calculating internal radiance fields. When the underlying surface ($z = b$) has a known reflectance, and hence emittance, the upwelling radiance $\mathbf{N}^+(b)$ at the lower boundary has to be determined because of the presence of multiply scattered radiation between the medium and the surface. With no diffuse radiation entering the upper boundary ($z = 0$), the application of the interaction principle yields

$$\mathbf{N}^+(b) = \mathbf{R}_g \mathbf{V}^-(b) + \mathbf{R}_g \mathbf{N}^{\mathrm{dir}}(b) + (\hat{\mathbf{I}} - \mathbf{R}_g)B(T_g), \tag{A1}$$

$$\mathbf{V}^-(b) = \mathbf{R}(b, 0)\mathbf{N}^+(b) + \mathbf{R}(b, 0)(\hat{\mathbf{I}} - \mathbf{R}_g)B(T_g), \tag{A2}$$

where $B(T_g)$ is the Planck function associated with surface temperature T_g, $\mathbf{R}_g$ is the surface reflectance matrix, $\hat{\mathbf{I}}$ is the unit matrix, $\mathbf{N}^{\mathrm{dir}}$ and $\mathbf{V}^-$ are the direct and diffuse radiance vectors, respectively, and $\mathbf{R}(b, 0)$ is the reflectance matrix of the cloud layer. Substituting (A2) into (A1) yields

$$\mathbf{N}^+(b) = (\hat{\mathbf{I}} - \mathbf{R}_g\mathbf{R}(b, 0))^{-1}[(\hat{\mathbf{I}} + \mathbf{R}_g\mathbf{R}(b, 0))$$
$$\times (\hat{\mathbf{I}} - \mathbf{R}_g)B(T_g) + \mathbf{R}_g\mathbf{N}^{\mathrm{dir}}(b)]. \tag{A3}$$

To obtain the spectral heating and cooling rates [cf. Eq. (1)] of a medium requires the flux divergence

$$\nabla \cdot \mathbf{F}. \tag{A4}$$

The irradiance $\mathbf{F}$ is calculated from the radiative transfer equation

$$\boldsymbol{\xi} \cdot \nabla I(\mathbf{r}; \mu, \phi) = -\alpha(\mathbf{r})I(\mathbf{r}; \mu, \phi)$$
$$+ s(\mathbf{r}) \int_0^{2\pi} d\phi' \int_{-1}^1 P(\mathbf{r}; \mu, \phi, \mu', \phi')$$
$$\times I(\mathbf{r}; \mu', \phi')d\mu' + Q(\mathbf{r}; \mu, \phi), \tag{A5}$$

where $I(\mathbf{r}; \mu, \phi)$ is the radiance, $\alpha(\mathbf{r})$ and $s(\mathbf{r})$ are the extinction and scattering functions, respectively, and $P(\mathbf{r}; \mu, \phi, \mu', \phi')$ is the phase function. The term $Q(\mathbf{r}; \mu, \phi)$ appearing on the right-hand side of (A5) is the internal source function. In the thermal radiation regime, when local thermal equilibrium is established, the spectral emissivity $k(\mathbf{r}) = \alpha(\mathbf{r}) - s(\mathbf{r})$ and the source function is given by

$$Q(\mathbf{r}; \mu, \phi) = k(\mathbf{r})B[T(\mathbf{r})], \tag{A6}$$

where $B[T(\mathbf{r})]$ is the Planck function at temperature $T(\mathbf{r})$. In addition, if the medium is illuminated by solar radiation, the total radiance required for the calculation of the flux divergence must include not only the diffuse radiance $I(\mathbf{r}; \mu, \phi)$, but also the direct solar radiance $I^0(\mathbf{r}; \mu_0, \phi_0)$ as well. The total radiance (I^T) is

$$I^T(\mathbf{r}; \mu, \phi) = I(\mathbf{r}; \mu, \phi)$$
$$+ \delta(\mu - \mu_0)\delta(\phi - \phi_0)I^0(\mathbf{r}; \mu_0, \phi_0). \tag{A7}$$

Inserting (A6) and (A7) into (A5), and integrating μ and ϕ over $4\pi sr$, yields

$$-\nabla \cdot \mathbf{F} = k(\mathbf{r})\{4\pi\bar{I}(\mathbf{r})$$
$$+ I^0(\mathbf{r}; \mu_0, \phi_0) - 4\pi B[T(\mathbf{r})]\}, \tag{A8}$$

where

$$\bar{I}(\mathbf{r}) = \frac{1}{4\pi} \int_0^{2\pi} \int_{-1}^1 I(\mathbf{r}; \mu, \phi)d\mu d\phi. \tag{A9}$$

Equation (A9) defines the mean radiance. The direct radiance $I^0(\mathbf{r}; \mu_0, \phi_0)$ is best calculated by evaluating the exponential of the optical pathlength $\tau(\mathbf{r})$. Hence,

$$-\nabla \cdot \mathbf{F} = k(\mathbf{r})\{4\pi\bar{I}(\mathbf{r})$$
$$+ F_0\pi\mu_0 \exp(-\tau(\mathbf{r})) - 4\pi B[T(\mathbf{r})]\}. \tag{A10}$$

The above extensions were tested by employing various cloud extinction and scattering functions. Results compared well with those produced by the Spherical Harmonic Spatial Grid model of Evans (1993). It was noted, however, that the flux divergences obtained by including the thermal source function alone could differ by large amounts, even though the relative errors in the mean intensity were small. Thus, when the mean intensity is comparable to the Planck function, the accuracy of $\bar{I}(\mathbf{r}) - B[T(\mathbf{r})]$ is limited by round-off errors. These errors can become significant because they are magnified by the factor $4\pi k(\mathbf{r})$.

REFERENCES

Ackerman, S. A., and S. K. Cox, 1981: Aircraft observation of the shortwave fractional absorptance of non-homogeneous clouds. *J. Appl. Meteor.,* **20,** 1510–1515.

Arnott, W. P., Y. Y. Dong, and J. Hallett, 1994: Role of small crystals in radiative properties of cirrus: A case study, FIRE II, November 22, 1991. *J. Geophys. Res.,* **99,** 1371–1381.

Barton, I., 1983: Upper level cloud climatology from an orbiting satellite. *J. Atmos. Sci.,* **40,** 435–447.

Cahalan, R. F., W. Ridgway, W. J. Wiscombe, T. L. Bell, and J. B. Snider, 1994: The albedo of fractal stratocumulus clouds. *J. Atmos. Sci.,* **51,** 2434–2455.

Evans, K. F., 1993: Two-dimensional radiative transfer in cloudy atmospheres: The spherical harmonic spatial grid method. *J. Atmos. Sci.,* **50,** 3111–3124.

Gabriel, P. M., and K. F. Evans, 1996: Domain averaged solar radiative fluxes calculated by first order closures in two-dimensional media. *J. Atmos. Sci.,* **53,** 858–877.

——, S. C. Tsay, and G. L. Stephens, 1993: A Fourier-Riccati approach to radiative transfer. Part I: Foundations. *J. Atmos. Sci.,* **50,** 3125–3147.

Gao, B. C., A. F. H. Goetz, and W. J. Wiscombe, 1993: Cirrus cloud detection from airborne imaging spectrometer data using the 1.38 µm water vapor band. *Geophys. Res. Lett.,* **20,** 301–304.

Goody, R. M., R. West, L. Chen, and D. Crisp, 1989: The correlated-*k* method for radiation calculation in nonhomogeneous atmospheres. *J. Quant. Spectrosc. Radiat. Transfer,* **42,** 539–550.

Harshvardhan, and J. A. Weinman, 1982: Infrared radiative transfer through a regular array of cuboidal clouds. *J. Atmos. Sci.,* **39,** 431–439.

Hayasaka, T., K. Nobuyuki, and M. Tanaka, 1995: Absorption of solar radiation by stratocumulus clouds: Aircraft measurements and theoretical calculations. *J. Appl. Meteor.,* **34,** 1047–1055.

Heymsfield, A. J., K. M. Miller, and J. D. Spinhirne, 1990: The 27–28 October 1986 FIRE IFO cirrus case study: Cloud microstructure. *Mon. Wea. Rev.,* **118,** 2313–2328.

King, M. D., 1987: Determination of the scaled optical thickness of clouds from reflected solar radiation measurements. *J. Atmos. Sci.,* **44,** 1734–1751.

——, Y. J. Kaufman, W. P. Menzel, and D. Tanré, 1992: Remote sensing of cloud, aerosol, and water vapor properties from the Moderate Resolution Imaging Spectrometer (MODIS). *IEEE Trans. Geosci. Remote Sens.,* **30,** 2–27.

——, and Coauthors, 1996: Airborne scanning spectrometer for remote sensing of cloud, aerosol, water vapor and surface properties. *J. Atmos. Oceanic Technol.,* **13,** 777–794.

Liou, K. N., 1986: Influence of cirrus clouds on weather and climate processes: A global perspective. *Mon. Wea. Rev.,* **114,** 1167–1199.

McClatchey, R. A., R. W. Fenn, J. E. A. Selby, F. E. Volz, and J. S. Garing, 1972: Optical properties of the atmospheres. Rep. AFCRL-72-0497, Air Force Cambridge Res. Lab., Bedford, MA, 108 pp.

Nakajima, T., and M. D. King, 1990: Determination of the optical thickness and effective particle radius of clouds from reflected solar radiation measurements. Part I: Theory. *J. Atmos. Sci.,* **47,** 1878–1893.

Price, R. D., M. D. King, J. T. Dalton, K. S. Pedelty, P. E. Ardanuy, and M. K. Hobish, 1994: Earth science data for all: EOS and the EOS Data and Information System. *Photogramm. Eng. Remote Sens.,* **60,** 277–285.

Salomonson, V. V., W. L. Barnes, P. W. Maymon, H. E. Montgomery, and H. Ostrow, 1989: MODIS: Advanced facility instrument for studies of the earth as a system. *IEEE Trans. Geosci. Remote Sens.,* **27,** 145–153.

Sassen, K., C. J. Grund, J. D. Spinhirne, M. M. Hardesty, and J. M. Alvarez, 1990: The 27–28 October 1986 FIRE IFO cirrus case study: A five lidar overview of cloud structure and evolution. *Mon. Wea. Rev.,* **118,** 2288–2311.

Spinhirne, J. D., M. Z. Hansen, and L. O. Caudill, 1982: Cloud top remote sensing by airborne lidar. *Appl. Opt.,* **22,** 1564–1571.

——, H. J. Zwally, R. H. Thomas, C. R. Bentley, B. E. Schutz, and S. T. Shipley, 1991: Climate measurements by the EOS Geoscience Laser Ranging System. *Second Symp. on Global Change Studies,* New Orleans, LA, Amer. Meteor. Soc., 17–22.

——, W. D. Hart, and D. L. Hlavka, 1996: Cirrus infrared parameters and shortwave reflectance relations from observations. *J. Atmos. Sci.,* **53,** 1438–1458.

Stackhouse, P. W., Jr., and G. L. Stephens, 1991: A theoretical and observational study of the radiative properties of cirrus: Results from FIRE. *J. Atmos. Sci.,* **48,** 2044–2059.

Starr, D. O., and S. K. Cox, 1985: Cirrus clouds. Part II: Numerical experiments on the formation and maintenance of cirrus. *J. Atmos. Sci.,* **42,** 2682–2694.

Stephens, G. L., and R. W. Preisendorfer, 1984: Multimode radiative transfer in finite optical media. Part II: Solutions. *J. Atmos. Sci.,* **41,** 725–735.

——, S. C. Tsay, P. W. Stackhouse Jr., and P. J. Flatau, 1990: The relevance of the microphysical and radiative properties of cirrus clouds to climate and climatic feedback. *J. Atmos. Sci.,* **47,** 1742–1753.

Takano, Y., and K. N. Liou, 1995: Radiative transfer in cirrus clouds. Part III: Light scattering by irregular ice crystals. *J. Atmos. Sci.,* **52,** 818–837.

Webster, P. J., and G. L. Stephens, 1980: Tropical upper-tropospheric extended clouds: Infrences from winter MONEX. *J. Atmos. Sci.,* **37,** 1521–1541.

Wielicki, B. A., and Coauthors, 1990: The 27–28 October 1986 FIRE IFO cirrus case study: Comparison of radiative transfer theory with observations by satellite and aircraft. *Mon. Wea. Rev.,* **118,** 2356–2376.

——, R. D. Cess, M. D. King, D. A. Randall, and E. F. Harrison, 1995: Mission to planet earth: Role of clouds and radiation in climate. *Bull. Amer. Meteor. Soc.,* **76,** 2125–2153.